Measuring Rotational Degrees of Freedom Using a Laser Doppler Vibrometer

M. J. Ratcliffe

N. A. J. Lieven

Department of Aerospace Engineering,
University of Bristol,
Bristol BS8 1TR, UK

Many model updating and dynamic coupling techniques require the response of a structure to be defined at all degrees of freedom. Standard experimental techniques do not routinely allow the measurement of rotational DoFs. Also time constraints do not permit measurement over a dense grid. A laser system has been developed which enables rotations to be extracted by a simple plane-fitting technique, which is described in this paper. A finite element model-based parametric study is presented, which has shown that the performance of the technique is dependent on the amount of corruption present on translation data.

A semi-empirical technique is developed, using second derivatives to exacerbate temporarily the noise corruption, which quantifies accurately the equivalent Gaussian noise on the response data. An experimental study is also presented which shows the considerable promise of these procedures. Finally, a brief description of a model updating case study is presented for illustrative purposes.

Terminology

In order to avoid a verbose sentence construction, the coordinate at which it is desired to measure the rotational frequency response functions (FRFs) is hereafter referred to as the rotation point. *In addition, the distance between the measured translation FRFs and the rotation point is referred to as the* measurement radius.

1 Introduction

Current model updating routines [1–3] and FRF coupling techniques [4] require that the response of a structure be defined at all degrees of freedom (DoFs). Traditional techniques for experimental determination of responses are effective only for translational and a very limited subset of rotational DoFs. Practical considerations tend to mean that the experimental response set is limited only to the out-of-plane translations. Theoretical methods exist which attempt either to expand the experimental data sets to incorporate the extra DoFs [5], or to reduce the size of the finite-element model [6]. This paper presents a technique that uses the simple expedient of fitting a plane in a least-squares sense to experimental translation data—which are measured in a circle around the rotation point—to calculate the two out-of-plane rotations.

2 Laser Doppler Anemometry

A PC-based system to drive a Laser Doppler Velocimeter (LDV) has been developed specifically for the purposes of dynamic finite element model updating. This apparatus enables the acquisition of FRF data with a much denser measurement grid than would normally be the case, because of its speed of operation; this fact, together with the exceptional purity of data afforded by the state-of-the-art LDV system, is essential to the workings of the technique presented in this paper. The system can be programmed to scan automatically through a geometry file, and therefore requires little interactive supervision.

Laser techniques work using the Doppler effect: when light contacts a moving surface, the frequency of the reflected beam is altered by an amount $2\nu/\lambda$, where λ is the wavelength of the light, and ν is the velocity of the surface. The laser beam is split into two parts, with one half arranged to fall on the structure at a single point. The other half is used as a reference beam and is allowed to interfere constructively and destructively with the measurement beam, which has been reflected back by the structure. Changes in the intensity of the light can be measured using photodetectors, and this enables frequency shifts as small as 1 part in 10^{14}, equivalent to about μm per second, to be measured.

The LDV generally produces data of a quality superior to other measurement devices—such as accelerometers—and does not suffer from mass-loading effects. However, in certain conditions, extreme local noise effects can be caused by drop-out. Drop-out occurs when there is very little laser beam signal reflected back to the laser measurement system. Drop-out can be reduced by using a retroreflective material that will reflect back over a large arc, and is available in paint or adhesive-tape form; the present work uses retroreflective tape to produce diffuse reflections.

3 Least-Squares Plane Fitting in Three Dimensions

Conventional least-squares fitting techniques involve analytical differentiation to minimise the squared difference between the desired line or plane and the noisy experimental data. Analytical differentiation, although often trivial, cannot easily be performed by a computational algorithm, so the alternative approach shown below is used.

The equation of a plane in three-dimensional space is:

$$z = Ax + By + C \tag{1}$$

A and B are the gradients of the plane, which correspond to the rotations that the method is designed to measure. The constant, C, which is the point at which the plane crosses the z-axis can be removed by moving the origin of the space, using the fact that the plane is sure to pass through the spatial centre of gravity of the data, i.e.

$$\hat{X}_i = X_i - \bar{X}$$

$$\hat{Y}_i = Y_i - \bar{Y}$$

$$\hat{Z}_i = Z_i - \bar{Z} \tag{2}$$

Contributed by the Technical Committee on Vibration and Sound for publication in the Journal of Vibration and Acoustics. Manuscript received May 1996; revised May 1997. Associate Technical Editor: J. Mottershead.

We want to find:

$$\sum \tfrac{1}{2}(A\hat{X}_i + B\hat{Y}_i - \hat{Z}_i)^2\big|_{\min} \tag{3}$$

Differentiating with respect to A to find the best gradient in the Y-direction

$$\sum (A\hat{X}_i + B\hat{Y}_i - \hat{Z}_i)\hat{X}_i = 0 \tag{4}$$

Differentiating with respect to B to find the best gradient in the X-direction

$$\sum (A\hat{X}_i + B\hat{Y}_i - \hat{Z}_i)\hat{Y}_i = 0 \tag{5}$$

These two expressions can be rearranged, using simple algebra, to form:

$$A = \frac{\sum \hat{Y}_i^2 \sum \hat{X}_i\hat{Z}_i - \sum \hat{Y}_i\hat{Z}_i \sum \hat{X}_i\hat{Y}_i}{-\sum \hat{X}_i\hat{Y}_i \sum \hat{X}_i\hat{Y}_i + \sum \hat{X}_i^2 \sum \hat{Y}_i^2} \tag{6}$$

$$B = \frac{\sum \hat{X}_i\hat{Z}_i \sum \hat{X}_i\hat{Y}_i - \sum \hat{X}_i^2 \sum \hat{Y}_i\hat{Z}_i}{\sum \hat{X}_i\hat{Y}_i \sum \hat{X}_i\hat{Y}_i - \sum \hat{X}_i^2 \sum \hat{Y}_i^2}. \tag{7}$$

This gives us a straight-forward method for extracting out-of-plane rotations from translation data: simply measure translation FRFs at coordinates close to the rotation point. Once the plane has been fitted to the data, it is a simple matter to calculate the angular displacement. Clearly, the accuracy of the method is determined by the distance between the points where the translations are measured. Conventional experimental techniques use too coarse a grid to attain sufficient accuracy. Laser Doppler techniques, however, have the advantage of a very small measurement area, as well as providing the capability of measuring a structure using a much finer grid because of their speed of operation.

4 Finite Element Model Case Study

Intuitively, one would expect the accuracy of the plane fit technique to decrease the further the translation FRFs are away from the rotation point because of the curvature of the displacement shape. However, errors manifest in vibration test data will degrade the performance of the plane-fitting procedure, and the effect of random noise errors will *increase* at small distances.

An FE model case study was undertaken in order to quantify the effects of noise corruption and the behaviour of the procedure when the measurement radius is varied. The model chosen for this investigation was a free-free plate—which typified a civil aircraft wing—of uniform thickness and is shown in Fig. 1. It was anticipated that this structure would be sufficiently complex to demonstrate procedural limitations, while being simple enough to afford excellent correlation with a genuine experiment. Note in particular the dense structure of the FE model around a node in mid-chord, just outboard of the wing crank. This is the node that was examined in detail, and the dense modelling was necessary—albeit artificially elaborate—to enable the requisite FRFs to be generated. The experimental study is discussed below in section 8.

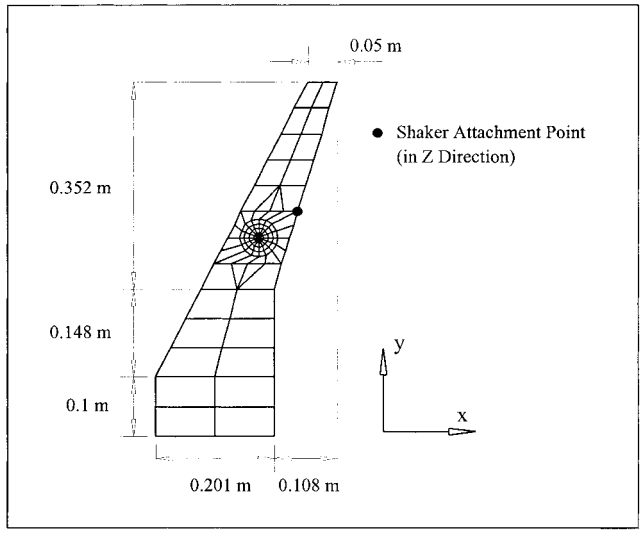

Fig. 1 Case study FE model, showing dense node structure, and experimental shaker attachment point

The FRFs were generated by inverting the dynamic stiffness matrix, i.e.:

$$\alpha(\omega) = ([K] - \omega^2[M])^{-1} \tag{8}$$

where each individual FRF is given by a single element of the receptance matrix. This method of producing the FRFs is more expensive, both in terms of run-time and storage space required, than regenerating them from a linear combination of modes, but it was chosen in order to guarantee no modal truncation took place [4].

Figure 2 shows the effects of increasing the distance and, as expected, there is significant variation in the FRF estimates as the distance increases. The amount of variation is frequency dependent and clearly increases with frequency; this is to be expected since local curvature is greater for higher order modes. Although the differences are considerably more marked at higher frequencies, low order modes are more important for most modal analysis applications. It is interesting to note that there appears to be a greater improvement in the θ_x rotation FRF (particularly close to anti-resonances) than in the θ_y rotation FRF. This is a case-specific phenomenon that is explained later.

Figure 2 is difficult to interpret because there is no quantitative measure of the error on the FRF curves. Therefore, the *Normalized Response Difference* [5] is used to quantify the accuracy of the FRF approximation.

$$NRD(\{\alpha_A\}, \{\alpha_X\}) = \frac{\|\{\alpha_A\} - \{\alpha_X\}\|_2}{\|\{\alpha_A\}\|_2} \tag{9}$$

If the FRF data are analytical and therefore not contaminated in any way by the effects of experimental noise, then the error will

Nomenclature

a = normally distributed variable
A, B, C = plane fitting constants (gradients in X, Y & Z respectively)
$[H]$ = hysteretic damping matrix
$[K]$ = stiffness matrix
MAC = modal assurance criterion
MSF = modal scale factor
NRD = normalized response difference
R = roughness
R_α = receptance roughness
s = standard deviation
x, y = Cartesian coordinates
X_i, Y_i, Z_i = data points in 3D space
$\bar{X}, \bar{Y}, \bar{Z}$ = center of gravity of data
$\hat{X}, \hat{Y}, \hat{Z}$ = shifted data
$\alpha\omega$ = FRF datum
α_A = analytical FRF
α_X = experimental FRF
ϕ_A = analytical modeshape vector
ϕ_X = experimental modeshape vector
∇^2 = Laplacian operator
$\|\nu\|_2$ = 2-norm of any vector, ν

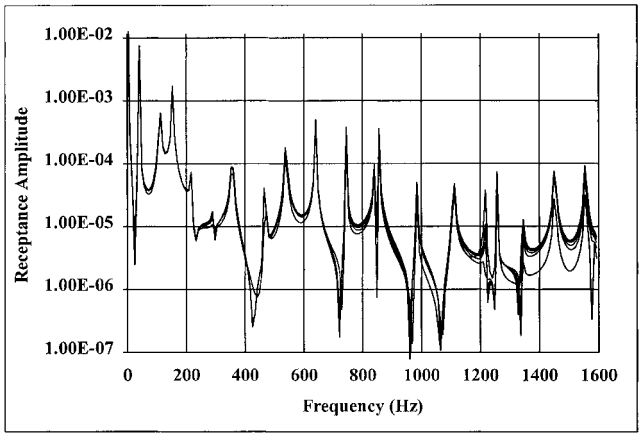

Fig. 2(*a*) Analytical rotation estimations, θ_x rotation

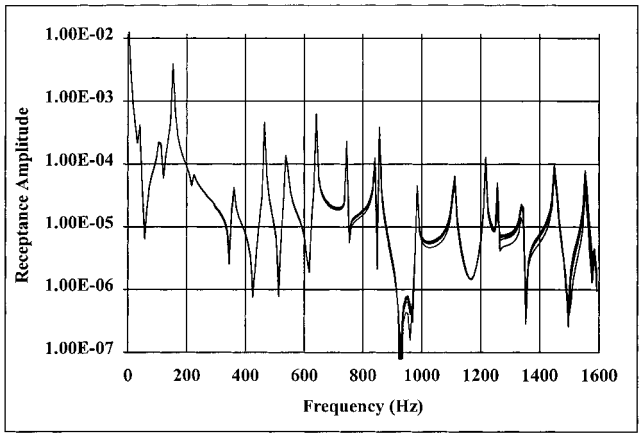

Fig. 2(*b*) Analytical rotation estimations, θ_y rotation

decrease monotonically with reduced distance from the rotation point. This ideal case is not representative of real FRFs, however, and is therefore not considered any further in this work. A simple Gaussian distribution is chosen to corrupt the data; each data point is factored as follows:

$$\alpha(\omega) = \alpha(\omega)(1 + a \cdot s) \tag{10}$$

where a is a normally distributed variable, and s is a user-specified standard deviation. This noise model is not truly representative of the noise contamination manifest on a true experimental test, and more sophisticated models do exist that produce more realistic noise distributions, and realistic-looking coherence estimates [7]. Cobb's noise model includes noise as absolute values, rather than the simple proportional distribution used in this work. However, Cobb's work assumes three different regions where noise influences the measurement process:

- an input noise, between the desired input signal and the true input signal;
- a force transduction error between the measured input force and the true input force; and
- an output error between the measured output and the true output.

In section 6, an attempt is made to estimate the amount of noise corruption present on FRFs. This procedure would become unnecessarily unwieldy if the noise was described by three parameters, as in Cobb's work. The simple proportional noise model is ideal for this work because the amount of noise corruption is determined by a single parameter.

The final error is expected to be a function of both the distance from the rotation point, and the amount of noise corrupting the data, and this result is clearly shown in Fig. 3(*a*).

This figure was generated by computing analytical translation FRFs at different measurement radii. Then differing amounts of Gaussian noise were added to the FRFs, and the rotations were derived from the corrupted data. The accuracy of each rotational FRF was then assessed through use of the NRD. For each amount of added noise the minimum error is marked with a circle.

There is a surprising amount of scatter in Fig. 3. This can be explained by considering two aspects of the way that the case study was carried out: firstly, the structure's modes at the frequencies considered have relatively low curvature. Secondly, because there is no reason to assume *exactly* the same amount of random corruption for different points on the structure, a different random seed was used for each translation FRF in the simulation.

It is also interesting to note that the NRD error values for the θ_x FRFs are generally larger than for the equivalent θ_y rotations, and seem more sensitive to the measurement radius. This case-specific result—which was mentioned in passing above—is due to the modal properties of the wing model. The modes up to 400 Hz are predominately bending in nature, and in particular, no torsion mode at these low frequencies involves a bending about the center chord of the wing. This means that the wing section is less highly curved in the y-direction, and therefore the plane-fit is more accurate. The θ_y FRF is less sensitive to the measurement radius for the same reason.

Figure 3(*b*) shows "plan views" of the error distributions for, respectively four, eight and sixteen measurement points and shows

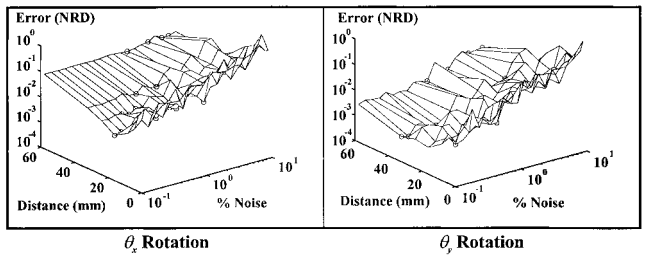

Fig. 3(*a*) The variation of optimum measurement radius with added Gaussian noise

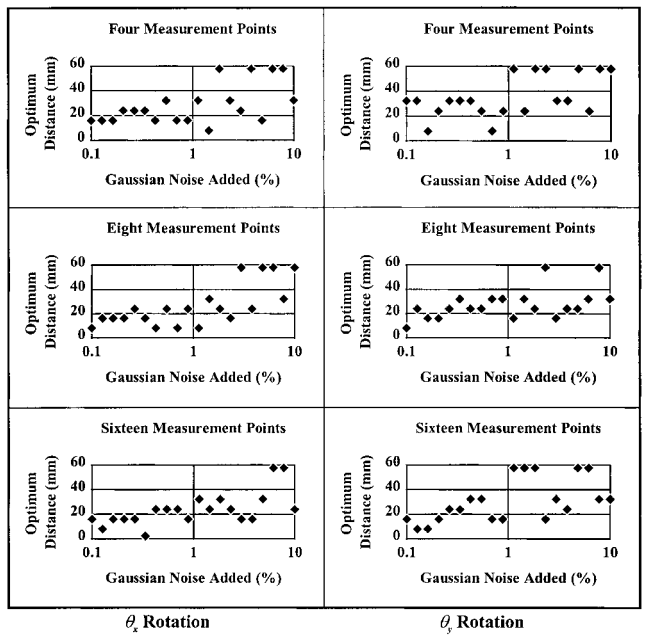

Fig. 3(*b*) Optimum measurement radii for differing numbers of measured points

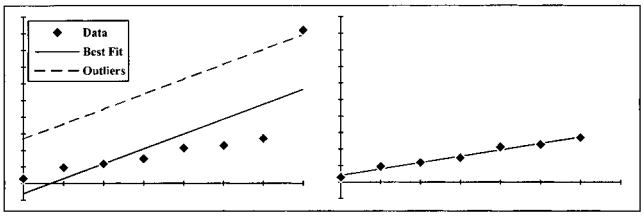

Fig. 4 Simple demonstration of outliers

more clearly the positions of minimum error for each value of noise, which are denoted by the marker on these figures. It is interesting to note that the optimum measurement radius decreases with an increased number of points. This is because the plane fit is better defined by the extra number of measurement points.

It can be concluded from Fig. 3(*b*) that the optimum measurement radius is approximately 16 mm for this case study. However, it is important to be aware that a compromise would have to be reached if trying to measure rotations near a corner of a structure, if the internal angle is less than 90 deg. This is because only a small arc would be available for measurement, and the measurement points would be very close together.

5 Outlier Removal

An advantage of the plane-fitting technique is that it allows the location and removal of outlying points. An outlier is a data point which—for any reason—is particularly distant from related points. Such a datum can significantly degrade the accuracy of a least-squares fit, since the solution is dominated by the points with largest error. This effect is demonstrated in Fig. 4. The left-hand graph shows eight data points, with one point considerably distant from the others. The solid line shows the least-squares fit, and it is significantly worse than optimum. A dashed line is shown at $+3\sigma$, which is a common definition of an outlier, and the anomalous point is seen to lie outside this region. The deviations from the plane are defined in the same way as standard deviation from the mean of a statistical distribution, i.e.:

$$\sigma^2 = \frac{1}{N}\sum_{i=1}^{N} \delta_i^2 \tag{11}$$

where N is the number of points, and δ is an individual point's distance from the best-fit plane.

Removal of this point from the data set can improve the accuracy of the line-fit, as shown in the right hand side figure. Removal is straightforward; any point that is more than three standard deviations from the plane is excluded from the data used to calculate the rotational DoFs. The rotations are then re-calculated from $N - 1$ data points, instead of N points.

Outlier removal was coded into the plane-fitting algorithm, and the standard deviations from the plane were calculated at each frequency point. A demonstration of the improvement that this simple method can bring to bear on rotational FRFs is shown in Fig. 5. An inaccurate reading was simulated by adding 100 percent Gaussian noise to one FRF, and the corrupting effect on the plane fit is demonstrated by the disparity between the FRF traces. Such heavy corruption can occur sporadically when an LDV is used when laser light is not reflected sufficiently well to the laser sensor; this phenomenon is known as drop-out. Note that in order to focus entirely on the improvements possible by the removal of a single particularly anomalous point, all the other translational FRFs were noise-free.

When the anomalous data are removed automatically, the FRFs overlay as expected; however the perfect FRF is not quite reproduced, as there is a region of error around 300 Hz, which is the region where the fourth bending mode of the wing dominates. There is a region of low curvature near the node of interest, and so

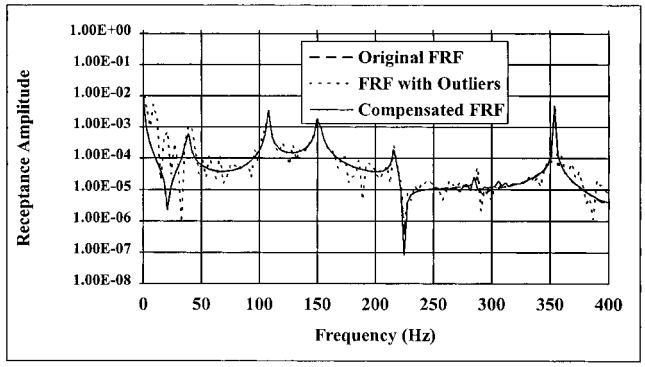

Fig. 5(*a*) Outlier removal, θ_x rotation

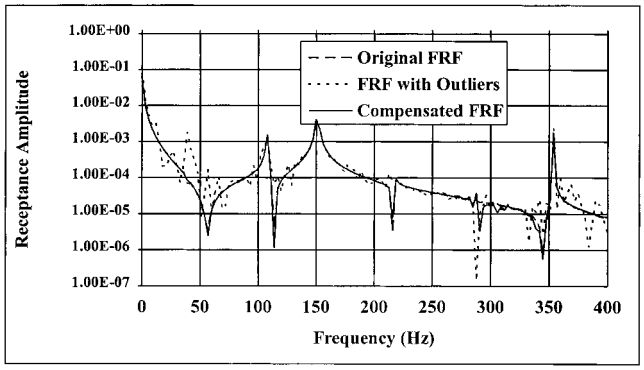

Fig. 5(*b*) Outlier removal, θ_y rotation

although the translation FRF has a large value, the rotational FRFs are small. The NRD is again used to calculate the disparities between the analytical and the regenerated rotations, and these results are presented in Table 1.

Note that the use of the Gaussian noise model does not influence the applicability of the outlier removal procedure. Any point that is distant from the plane will be omitted—whatever the source of noise.

Further interesting insight into the behavior of the plane-fitting technique can be obtained by plotting the deviations from the plane against frequency. Figure 6 shows the deviations for the analytical model, with no added noise, at a radius of 16 mm. It can be seen that the deviations from the plane are greatest at resonance, simply because of the fact that the response is greatest at those frequencies. The deviations are particularly large at the region around 300 Hz, and this is the reason that not all the outlying points in Fig. 7 were rejected. The standard deviations are so large with no added noise, that only the most disparate of data are discarded by the outlier removal.

The work presented above has shown that the optimum measurement radius is a function of the amount of noise on the FRFs, which is not known *a priori*, and has therefore demonstrated the need for a reliable estimate of the level of corruption present on response data. A technique is presented below which evaluates an approximation to the equivalent Gaussian noise present on FRFs.

Table 1 NRD values before and after outlier removal

	FRF with Outliers	Compensated FRF
θ_x Rotation	0.9470	0.0122
θ_y Rotation	0.4943	0.0024

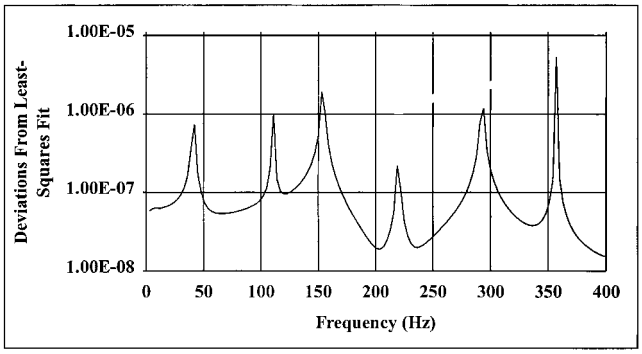

Fig. 6 Deviations from the plane-fit

6 Gaussian Noise Estimator

Waters [5] has defined a *roughness* parameter, defined at N FE grid points, that uses the Laplacian operator to evaluate an estimate of noise on modeshapes as:

$$R = \sum_{i=1}^{N} |\nabla^2 W(x_i, y_i)| \tag{12}$$

where $W(x, y)$ is a surface fit of measure response and:

$$\nabla^2 W(x, y) = \frac{\partial^2 W}{\partial x^2} + \frac{\partial^2 W}{\partial y^2}. \tag{13}$$

This method is extended here to the estimation of noise on frequency response functions.

A roughness parameter is calculated at every frequency point of interest, combining the translational receptance at every node to create a displacement shape. These roughness parameters are then summed over the frequency range to generate *receptance roughness.*

$$R_\alpha = \sum_{i=1}^{F} |R_i| \tag{14}$$

This measure is case-dependent, and the relationship between receptance roughness and Gaussian noise is not evident. Figure 7 shows receptance roughness plotted against the amount of Gaussian noise added to the FRFs. The values of receptance roughness are seen to increase with added noise, as expected, and in addition, the variance of the data is seen to increase with increased added noise. This phenomenon is a feature of the noise model, and is explained below. Figure 7 was generated as follows: twenty-five values for Gaussian noise were selected, and this amount of proportional noise was added to FRFs at every translational DoF. Receptance roughness was the calculated at each value of added noise. Because of the random nature of the added noise, there is some variation in the calculated values of receptance roughness for any value of added noise. For this reason, ten calculations were performed at each of twenty-five different amounts of added noise to enable a mean value curve to be drawn through the data, and it is this best-fit line which will be used in the noise estimation technique described below. The procedure for using the method for experimental data is shown in Table 2.

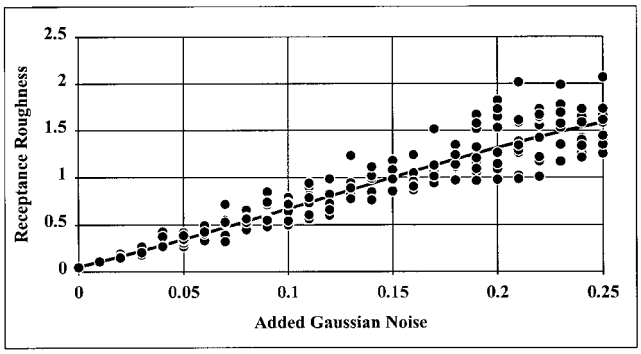

Fig. 7 Receptance roughness calculated at different levels of corruption

Table 2 Procedure for the estimation of equivalent Gaussian noise

Step	Action or Calculation
1	calculate a figure similar to figure 7 for the analytical model of the structure of interest;
2	generate the displacement shapes for the experimental model and scale them to correspond to the analytical model using the modal scale factor. This maps the experimental displacement shapes to approximately the same magnitude as the corresponding analytical shapes. Calculate the roughness values for each displacement shape. Then sum these values to create the experimental receptance roughness;
3	use the figure generated in 1. as a 'look-up' table to cross reference the calculated receptance roughness back to an estimate of the equivalent Gaussian noise present on the structure.

In principle, an equivalent estimator may be constructed from coherence values. However, such an estimator would suffer due to inadequacies of the proportional noise model, particularly at anti-resonance, where genuine experimental coherence tends to be low. This is because of the fact that noise dominates the response; a proportional noise model will not exhibit this property, since the noise *is* proportional, and will therefore not dominate at any frequency.

7 Noise Estimation Case Studies

Since there may be significant differences between the baseline FE model and the experimental model, it is necessary to test the applicability of the noise estimation technique to simulated *experimental* situations that are distinct from the FE model. Two different case studies were performed to assess the efficacy of the Laplacian-based technique, one case study representing an accurate FE model, and the other a more disparate theoretical model.

The lightly-perturbed model (hereafter referred to as *case 1*) was generated by factoring the mass of the wingtip and root elements by 140 percent, and factoring the stiffness of the mid-span elements by the same amount, as shown in Fig. 8. The error in the more disparate of the two test cases (*case 2*) was a uniform taper such that the thickness at the root of the model was changed from 3 mm to 3.6 mm, and the thickness at the wingtip was altered to 2.4 mm. The modes of these two test cases differ considerably from those of the unperturbed model as demonstrated by Table 3, which shows the Modal Assurance Criterion (MAC) values [8] between the test cases and the baseline model. The MAC values are the simplest method of assessing the difference between structural models.

The MAC is a commonly-used method of comparing modal vectors, and is typically used for estimating the amount of correlation between experimental and analytical modes. It is defined as:

$$MAC(\{\phi_X\}_i, \{\phi_A\}_j) = \frac{\left\|\{\phi_X\}_i^T \{\phi_A\}_j\right\|_2^2}{\{\phi_X\}_i^T \{\phi_X\}_i^* \{\phi_A\}_j^T \{\phi_A\}_j^*} \tag{15}$$

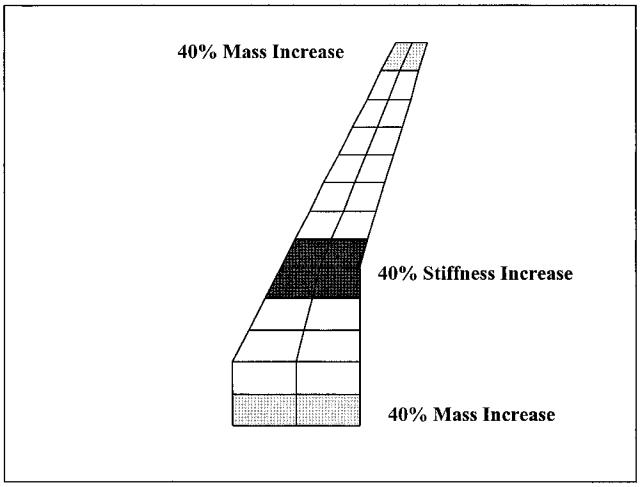

Fig. 8 Lightly perturbed model, case 1

It can clearly be seen that there is a significant degree of disparity between the two test cases and the baseline analytical model, and this is further demonstrated in Fig. 9, which shows the point receptances of the three models at a frequency range of 0–400 Hz.

7.1 Noise Estimation Results. Three plots of roughness against frequency for zero added noise are shown in Fig. 10; these demonstrate that the scaling via the MSF is working, and that while there are small areas of discrepancy (which represent poorly correlated displacement shapes at these frequencies), they tend to be at lower magnitudes. Note that the magnitude of the roughness is greatest at frequencies corresponding to the analytical resonances, as would be expected.

The rescaling of the displacement shapes via the MSF is an essential part of the technique for noise estimation. If it is not performed, differences in magnitude of displacement shape between different models could dominate the receptance roughness calculation. Large differences in magnitude could occur even if two models were extremely close because of the finite frequency resolution of testing. If one model has a resonance at a measured frequency line and another does not, then the magnitude of the response of the first model—and hence its receptance roughness—will be significantly larger than that of the second model.

Figure 11 shows estimated noise values, which have been generated as detailed in 6, above, plotted against Gaussian noise that was added to the starting FRFs, for both the lightly and strongly

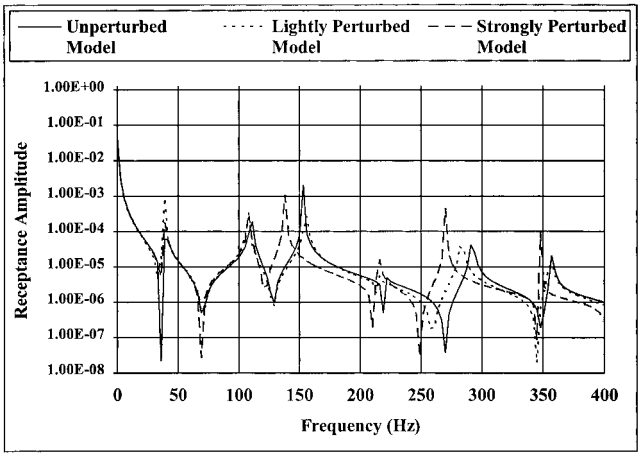

Fig. 9 Disparity between the test case models

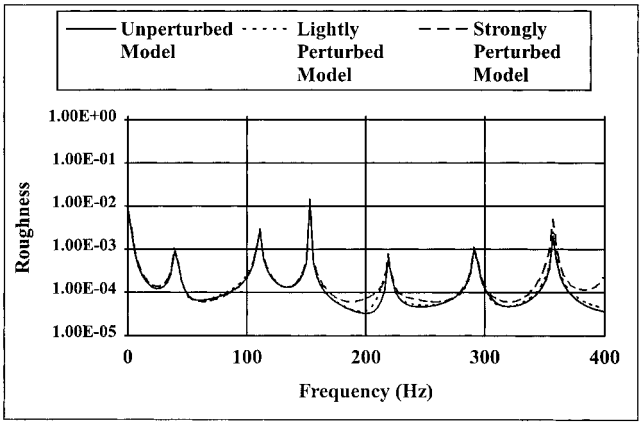

Fig. 10 Roughness disparity for the test case models

Table 3 MAC values between the perturbed case studies and the unperturbed baseline FE model

Mode	MAC		Nature of Mode
	Case 1	Case 2	
1	0.9975	0.9834	1st Bending
2	0.9967	0.9669	2nd Bending
3	0.9981	0.9897	1st Torsion
4	0.9928	0.9414	3rd Bending
5	0.9955	0.9710	4th Bending
6	0.9855	0.8637	2nd Torsion

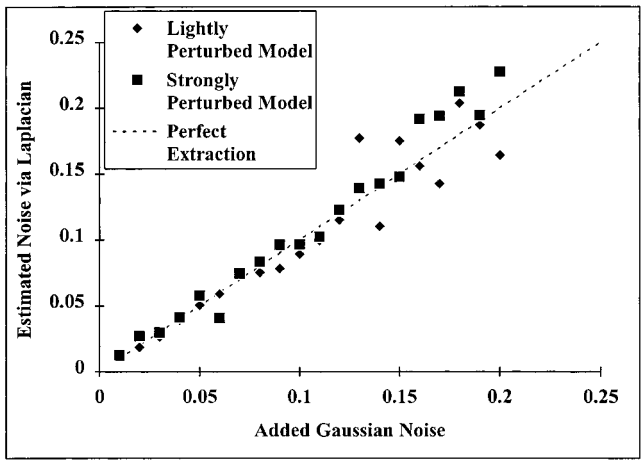

Fig. 11 Equivalent noise estimation

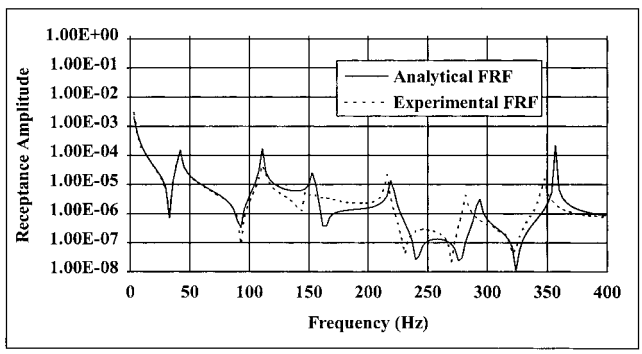

Fig. 12 Comparison of experimental and theoretical translation FRFs

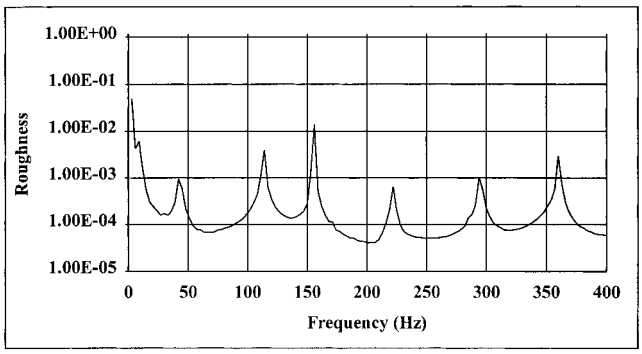

Fig. 13 Experimental roughness

perturbed models. The estimates are clustered around a line of unity gradient which represents a perfect noise estimation.

The performance of the method is seen to degrade slightly at higher levels of corruption, due to a number of factors:

- the rescaling via the MSF may have been upset;
- the receptance roughness is not a precise function of added noise, and the variance of the value calculated will increase with increasing corruption values; and
- a particular set of added Gaussian noise may have a greater corrupting effect on the data than another set of noise of the same standard deviation. This is a property of the Gaussian noise model.

In spite of the slight degradation of results at higher added noise levels, this represents an encouraging result. This technique enables the amount of corruption present on frequency response functions to be estimated accurately, and this has important implications in the selection of measurement radius as discussed in 4, above, and as shown in Fig. 2.

8 Experimental Study

While simulated case studies are invaluable in validating new techniques, real experimental tests must be performed in order to encompass the many unknown sources of error manifest in the real world. The uniform plate considered above in the finite element study was manufactured from 3 mm thick mild steel and suspended in a condition approaching free-free, on elastic cords. A pseudo-random excitation signal was applied to the structure via an electrodynamic shaker.

Rapid data acquisition is a prerequisite for this work; as an example of what can easily be achieved using an LDV, measurement of sixteen experimental FRFs, with ten averages, over the range 0–400 Hz with a frequency resolution of 0.5 Hz took approximately ten minutes. In addition, this procedure was fully automated, requiring little user interaction.

A comparison of two translation FRFs is presented in Fig. 12. These are the analytical and experimental translations at the rotation point, and thus it is hoped that they will display the anomalies between theory and experiment for this case. In particular, the resonance at approximately 150 Hz is poorly defined in the experimental data, due perhaps to structure-shaker interaction or some other effect that is not modelled in the FE analysis. At higher frequencies, some divergence in the natural frequencies can be observed. This is to be expected and is caused by the approximations inherent in the finite element modelling method. It is worth emphasising the exceptional quality of the data provided by the LDV system, which is a prerequisite of the method presented in this paper.

The receptance roughness for the structure was calculated from Fig. 13, which shows the roughness against frequency for this experimental study. The value was then cross-referenced back to Fig. 7, which gave a value of equivalent Gaussian noise of 1.04 percent. Figure 4 was then used, a measurement radius of 16 mm was selected, and sixteen points were measured around the node of interest.

The determination of the optimum measurement radius via the detailed FE study and the calculation of the amount of noise present on the data would not be practical for every measurement point. In particular the augmenting of the FE model with the dense modelling around a node of interest is particularly time-consuming. It is envisaged that experience could be gained rapidly so that a measurement radius could be chosen for a given experimental test set-up after only a few applications of this technique. The assumption would then be made that a particular region of a structure was subject to equal amounts of noise corruption for all measurement locations in that region.

Experimental rotations are overlaid with corresponding theoretical data in Fig. 14. This figure represents a very promising result. The anomalies present in the rotation FRFs can largely be traced back to inadequacies in the translation FRFs, such as that shown in the top of Fig. 12. The peculiarities around 150 Hz are caused by the corruption on the translation FRFs, mentioned above. Other anomalies are visible at low frequencies, where noise can be relatively large, and also around 300 Hz. This is a region of low curvature, as discussed above, and the measurement of a mode here is a genuine difference between theory and experiment, and therefore is an interesting result.

9 The Use of Complex Data in Rotation Measurements

The technique for the measurement of rotations described in this paper is readily extendible to complex FRF data by plane-fitting to the real and imaginary parts of the response data. However detailed analysis of optimum measurement radius, and the noise estimation procedure, becomes more difficult when dealing with imaginary data, because the imaginary component is zero away from resonance. The proportional noise model used in this work is not adequate for this situation, since it will not corrupt the data at all when the response is zero. This is unrepresentative of any genuine

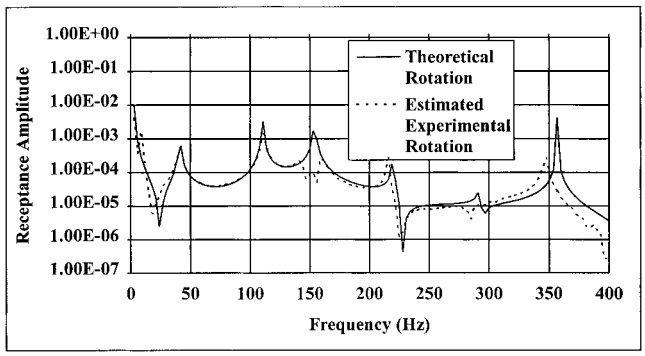

Fig. 14(*a*) Experimental and theoretical FRFs, θ_x rotation

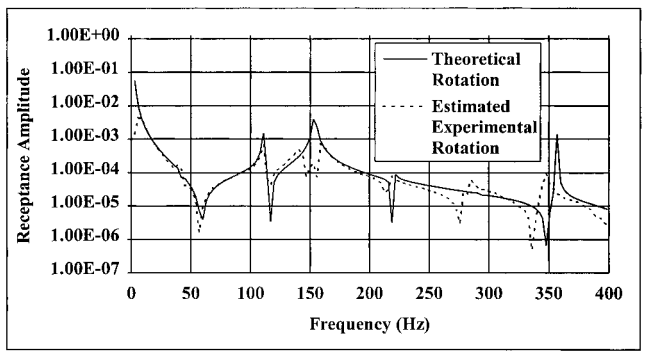

Fig. 14(*b*) Experimental and theoretical FRFs, θ_y rotation

Table 4 MAC [8] values between the analytical FE model and the tapered case study

Mode Number	MAC
1	0.9085
2	0.8536
3	0.9454
4	0.7531
5	0.8089
6	0.6897
7	0.7795
8	0.5243

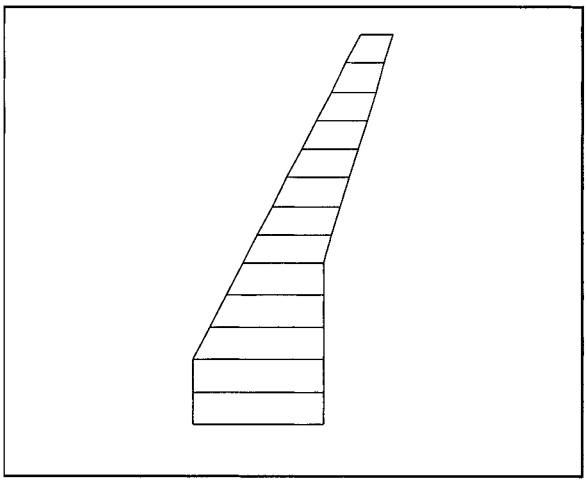

Fig. 15 Case study model showing macro element assignment

experiment, where the imaginary response is dominated by noise away from resonance.

10 The Effect of Rotational DoFs on FE Model Updating

A detailed updating study using rotational DoFs constitutes a large volume of work and is beyond the scope of this paper. This section presents a highly-condensed description of such a study [9] using the FRF sensitivity model updating technique [1, 5].

10.1 Case Study. The free-free wing section was again used as the basis for a case study into the effects of rotational DoFs. An *experimental* model was created by tapering the thickness of the uniform wing from 4.5 mm at the root to 1.5 mm at the tip. The modes of this *experimental* model differ considerably from those of the original model, as shown in Table 4.

The FRFs from the *experimental* model are corrupted with 10 percent Gaussian noise according to Eq. (10) and proportional hysteretic damping was added to the *experimental* model as shown.

$$[H] = \beta_H[K] \quad \text{where} \quad \beta_H = 0.005 \tag{16}$$

To improve the conditioning of the problem, macro elements are used. Macro elements in these cases were chosen in chordwise pairs, as shown in Fig. 15. This choice of updating parameters is consistent with the perturbations applied to create the *experimental* models; therefore, the updating parameters span the errors exactly, and in the absence of noise, a successful update will afford an exactly correct solution. A perfect solution is not possible if the choice of updating parameters is inadequate. The important topic of *p*-value selection is addressed in [9].

Previous work [5] has shown that the likelihood of a successful update is increased if high order frequencies are used. With this consideration in mind, one hundred frequency points were chosen, evenly distributed within the range 1–1200 Hz.

Two updating cases were run: one with only the *Z* DoFs available, and one with *Z*, θ_x and θ_y DoFs available. The unavailable *experimental* DoFs are replaced with the analytical DoFs by simple matrix mixing. Figure 16 shows the final solutions after ten iterations of the FRF sensitivity method together with the exact solutions. A small improvement is shown when the rotational DoFs are included; the mass and stiffness estimates are slightly more accurate when rotations are included, and the damping estimates are a significant improvement.

11 Concluding Remarks

A method for extracting rotations experimentally using the capacity of laser Doppler velocimetry for dense measurements has been presented. An FE study was conducted in order to determine optimum parameters for this calculation, and this has shown that measurement noise is critical to the performance of this procedure.

An innovative noise estimation procedure has been suggested.

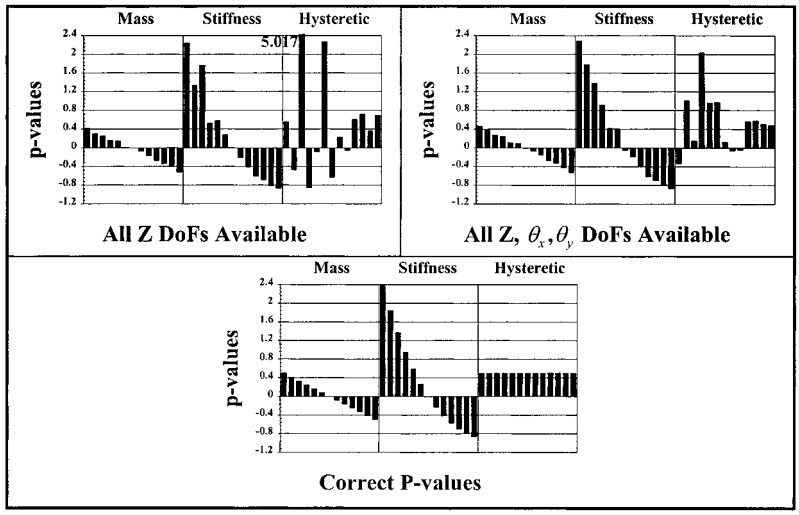

Fig. 16 Final *p*-values for 1.5– 4.5 mm tapaered wing, with 0.5 percent hysteretic damping, 10 percent noise

Promising results for this new technique were obtained when it was tested on two different FE case studies, and in addition, it yielded a realistic estimate of noise on the experimental case study.

By means of an experimental case study, it has been shown that laser velocimetry possesses the ability to extract accurate experimental rotations.

Brief results from an updating study using FRF sensitivity have been reported, and it has been shown that the inclusion of rotational DoFs yields a small, but significant improvement in the quality of results obtained.

12 References

1 Visser, W. J., and Imregun, M., "A Technique to Update Finite Element Models Using Frequency Response Data," IMAC IX, 1991, pp. 462–468.

2 Fissette, E., Stavrinidis, C., and Ibrahim, S., "Error Location and Updating of Analytical Dynamic Models Using a Force Balance Method," IMAC VI, 1988, pp. 1063–1070.

3 Lin, R. M., and He, J., "Analytical Model Improvement Using Modified IEM," *Proc. Structural Dynamics Modelling Test, Analysis and Correlation,* 1993, pp. 181–194.

4 Duarte, M. L. M., and Ewins, D. J., "Some Insights into the Importance of Rotational Degrees of Freedom and Residual Terms in Coupled Structure Analysis," IMAC XIII, 1995, pp. 164–170.

5 Waters, T. P., *Finite Element Model Updating Using Frequency Response Functions,* PhD Thesis, Department of Aerospace Engineering, University of Bristol, UK, 1995.

6 Guyan, R. J., "Reduction of Mass and Stiffness Matrices," *AIAA Journal,* Vol. 3, No. 2, 1965, p. 380.

7 Cobb, R. E., *Confidence Bands, Measurement Noise, and Multiple Input—Multiple Output Measurements Using the Three-Channel Frequency Response Function Estimator,* PhD Thesis, Department of Mechanical Engineering, Virginia Polytechnic Institute and State University, VA, USA, 1988.

8 Allemang, R. J., and Brown, D. L., "A Correlation Coefficient for Modal Vector Analysis," IMAC I, 1983, pp. 110–116.

9 Ratcliffe, M. J., and Lieven, N. A. J., "An Improved Method for Parameter Selection in Finite Element Model Updating," *The Aeronautical Journal,* Vol. 102, No. 1016, June/July 1998, pp. 321–329.